

Stellar neutron capture rates and the s process

F. Käppeler^{1,a}

Karlsruhe Institute of Technology (KIT), Campus North, Institute of Nuclear Physics,
76021 Karlsruhe, Germany

Abstract. Neutron reactions are responsible for the formation of the elements heavier than iron. The corresponding scenarios relate to helium burning in Red Giant stars (s process) and to supernova explosions (r and p processes). The s process, which operates in or near the valley of β -stability, has produced about half of the elemental abundances between Fe and Bi. Accurate (n, γ) cross sections are the essential input for s process studies, because they determine the abundances produced by that process. Following a brief summary of the neutron capture processes, the focus will be set on the s process in massive stars, where the role of reliable cross section information is particularly important. Eventually, the intriguing aspects of the origin of ^{60}Fe will be addressed. Attempts to determine the stellar cross section of that isotope are pushing experimental possibilities to their limits and present a pertinent challenge for future facilities.

1 Introduction

As introduced in the pioneering work by Burbidge, Burbidge, Fowler and Hoyle (B²FH) [1], the origin of the elements heavier than iron are ascribed to the slow and rapid neutron capture processes (s and r process), which are characterized by their typical time scales compared to average β -decay half lives. Both processes are contributing about half of the observed solar abundances between Fe and U. A third process, the so-called p (photodissociation) process, is responsible for the origin of about 30 rare, proton-rich nuclei, but does not contribute significantly to the synthesis of the elements in general (<1%). Since B²FH most progress has been made in the field of the s process, for which the contribution to the observed solar abundances could be quantified. It was found that there are at least two components, the main and the weak s process which are connected with the specific phases of stellar evolution. Initially, a third component, the strong s process, had been invoked for explaining part of the observed ^{208}Pb and ^{209}Bi abundances; this component was abandoned when it was understood that the main s process in low-metallicity stars can account for the missing fractions of ^{208}Pb and ^{209}Bi [2].

The main s process, by far the most studied process, occurs in the He-rich intershell of thermally pulsing AGB stars with $M \leq 3M_{\odot}$ and produces predominantly nuclei between ^{90}Zr and ^{209}Bi . At this stage, energy generation occurs by alternate episodes of radiative H burning and convective He burning in a comparably thin shell around the inert C/O core. Along with H burning, neutrons are liberated by the $^{13}\text{C}(\alpha, n)^{16}\text{O}$ reaction at temperatures of $T_8 \approx 1$ (T_8 means T in units of 10^8K), yielding neutron densities of about 10^7 cm^{-3} . Because there are only few seed nuclei in this thin shell, the neutron/seed ratio is high and the s process operates very efficiently over a long period of time. During the subsequent convective He flashes, the freshly synthesized material is mixed and diluted with the He intershell and is again exposed to neutrons liberated by the $^{22}\text{Ne}(\alpha, n)^{25}\text{Mg}$ reaction at temperatures $T_8 \approx 2.5$. The second neutron exposure is rather weak and not sufficient to produce s isotopes on a grand scale but strong enough to determine the isotope ratios of s -process branchings. After the He flash, where peak neutron densities of 10^{10} cm^{-3} are reached, part of the freshly synthesized

^a e-mail: franz.kaeppler@kit.edu

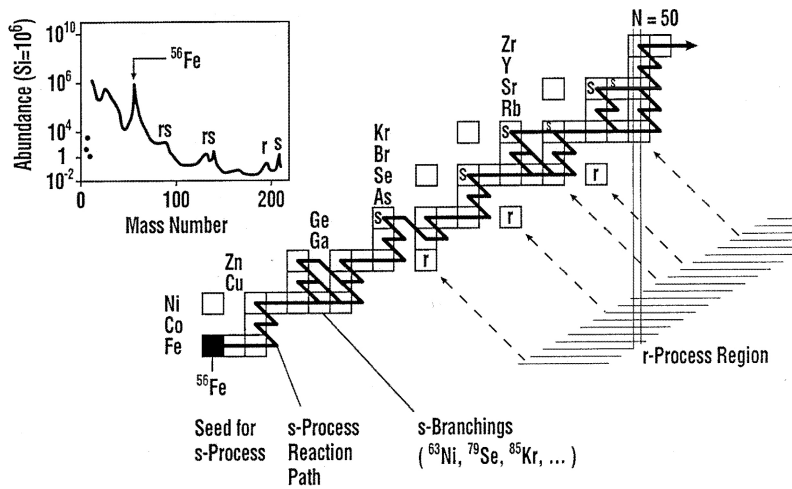


Fig. 1. Illustration of the neutron-capture processes responsible for the formation of the nuclei between iron and the actinides. Note that a p process has to be invoked for producing the proton-rich nuclei that are not reached by neutron-capture reactions. The schematic sketch of the solar abundance distribution in the inset indicates that the large abundance maximum in the Fe/Ni region represents the only relevant seed for the s process. The characteristic twin peaks in the abundance distribution between Fe and Pb result from the nuclear properties where the s - and r -reaction paths encounter magic neutron numbers.

material is mixed with the envelope and brought to the surface of the star, where it is detectable by optical spectroscopy.

The weak s component, which is responsible for the production of nuclei between iron and yttrium ($56 < A < 90$), takes place during convective core-He burning in massive stars ($M \geq 8M_{\odot}$), where temperatures reach $(2.2 - 3.5) \times 10^8$ K, thus marginally activating the $^{22}\text{Ne}(\alpha, n)^{25}\text{Mg}$ neutron source. Because the resulting neutron exposure is rather limited, the s -process reaction flow cannot overcome the bottleneck caused by the small cross sections of the isotopes with closed neutron shells at $N = 50$. However, most of the material in the core is reprocessed by the following burning stages and only a part survives in the outer layers and is ejected during the final supernova explosion. A second neutron exposure occurs during convective carbon shell burning in massive stars [3,4], where neutrons are produced mostly by the remaining $^{22}\text{Ne}(\alpha, n)^{25}\text{Mg}$, but also via $^{17}\text{O}(\alpha, n)^{20}\text{Ne}$ and $^{13}\text{C}(\alpha, n)^{16}\text{O}$. The high temperatures during carbon burning of $T_9 \approx 1$ cause high neutron densities, which start at about $10^{11} - 10^{12} \text{ cm}^{-3}$ and then decrease exponentially.

The nucleosynthesis yields of the weak component in massive stars are also important for the r process, since they determine the composition of a star before the supernova explosion. In contrast to the s process, where neutron capture times of the order of days to years confine the reaction path to or close to the valley of β stability, extremely high neutron densities of $\geq 10^{22} \text{ cm}^{-3}$ give rise to capture times of the order of ms, thus driving the reaction path to the region of very neutron-rich nuclei at the limits of stability. The reaction products of the explosive r process, which lasts for about a second, β -decay back to the valley of stability, where they mix with the s abundances.

The reaction paths of the s and r process are sketched in Fig. 1. The neutron-rich isotopes outside the s path can be ascribed to the r process. Apart from these r -only isotopes the r process contributes also to most of the other isotopes, except for those, which are shielded by stable isobars. The corresponding ensembles of s - and r -only isotopes are important for the separation of the respective abundance distributions. The subset of stable isotopes on the proton-rich side are attributed to the p process, which is likely to occur also in supernova explosions [5]. With a few exceptions, the p abundances are much smaller than the s and r components.

The decisive role of nuclear physics for a quantitative model of the s process was clearly expressed already by B²FH, who pointed out that the product of the stellar (n, γ) cross sections and of the resulting s abundances, $\langle \sigma \rangle N_s$, which represents the reaction flow, is a smooth function of mass number

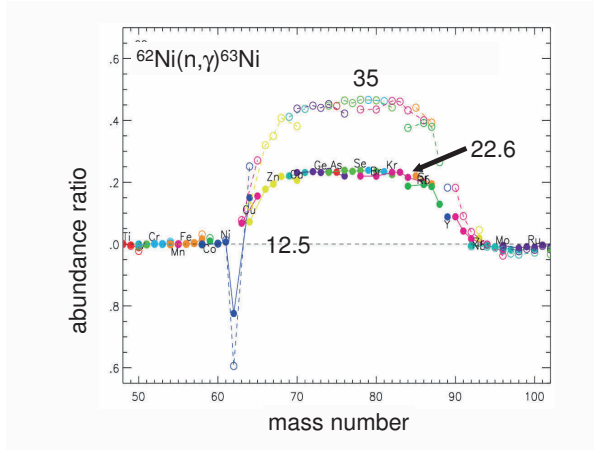


Fig. 2. Nucleosynthesis yields as a function of mass number calculated for a $25 M_{\odot}$ star normalized to the yields obtained with a ${}^{62}\text{Ni}(n, \gamma){}^{63}\text{Ni}$ cross section of 12.5 mbarn. Different values of the ${}^{62}\text{Ni}$ cross section give rise to a pronounced propagation effect on the entire abundance distribution of the weak s process. The cross section values are spanning the range of data obtained in recent experiments [6].

A. The steep decline of this function in the mass region of the weak s process between Fe and Y ($\approx 60 < A < 100$) indicates that the neutron supply per ${}^{56}\text{Fe}$ seed in massive stars is insufficient to build the s nuclei to their saturation abundances.

However, steady flow conditions have been reached in low mass stars, where the $\langle \sigma \rangle N_s$ function is practically constant in the mass region between Zr and Pb/Bi (apart from the neutron magic nuclei with $N = 50, 82$, and 128 , which act as bottle necks for the reaction flow because of their very small (n, γ) cross sections). This behavior implies that the s abundances are directly anti-correlated with the respective stellar cross sections.

The fact that flow equilibrium was not attained in massive stars has important consequences for the role of the stellar (n, γ) cross section in the mass region $60 < A < 90$. This is illustrated in Fig. 2 at the example of the ${}^{62}\text{Ni}$ cross section, which shows the very strong influence of a single cross section on the entire abundance distribution of the weak s process.

This propagation of cross section uncertainties has triggered increased experimental efforts as described in the following sections. In this mass region stellar neutron capture cross sections were mostly affected by uncertainties of more than 10%, but discrepancies between measurements were often much larger than the quoted uncertainties [6].

The stellar (n, γ) cross sections are obtained by folding the energy differential cross section with the thermal velocity distribution of the neutrons in the stellar plasma. These Maxwellian averaged cross sections (MACS) are defined as

$$\langle \sigma \rangle_{kT} = \frac{\langle \sigma v \rangle}{v_T} = \frac{2}{\sqrt{\pi}} \frac{\int_0^{\infty} \sigma(E_n) E_n e^{-E_n/kT} dE_n}{\int_0^{\infty} E_n e^{-E_n/kT} dE_n}. \quad (1)$$

where $E_n = E_n^{lab}(A/(A+1))$ denotes the total kinetic energy in the center-of-mass system, E_n^{lab} the laboratory neutron energy, $v_T = \sqrt{2kT/m}$ the mean thermal velocity, and m the reduced mass for the neutron-target system.

2 Activation measurements between Fe and Y

A first attempt at the Karlsruhe Van de Graaff to improve this situation was based on the activation technique [7]. Measurements were performed on a number of nuclei at the beginning of the s -process

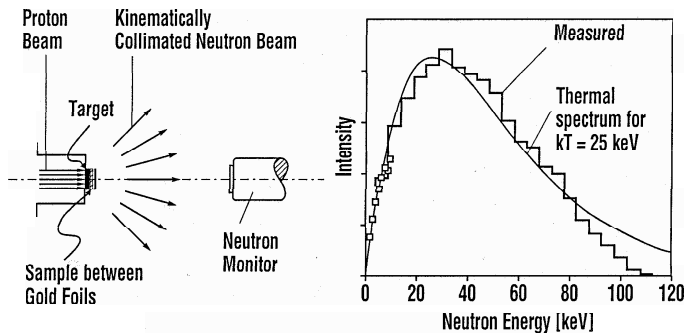


Fig. 3. Left: Schematic sketch of the activation setup. Right: The quasi-stellar neutron spectrum obtained with the ${}^7\text{Li}(n, \gamma){}^7\text{Be}$ reaction (histogram and symbols) compared to a true Maxwell-Boltzmann distribution for a thermal energy of $kT = 25$ keV. Note that the experimental spectrum falls below the Maxwell-Boltzmann distribution above 80 keV and contains no neutrons above 106 keV.

path, i.e., on ${}^{58}\text{Fe}$, ${}^{59}\text{Co}$, ${}^{64}\text{Ni}$, ${}^{63}\text{Cu}$, and ${}^{65}\text{Cu}$. These isotopes have in common that their stellar cross sections were all determined more than 20 years ago and that they have relatively small cross sections of less than 100 mbarn. This last point is crucial, because the smaller the cross section the more difficult it is to measure on one hand but the larger is the propagation effect in the final abundance distribution on the other.

The activation method represents a well established and accurate approach to determine MACSs at $kT = 25$ keV by producing a quasi-stellar neutron spectrum via the ${}^7\text{Li}(p, n){}^7\text{Be}$ reaction [8,9], which is obtained by using a proton beam energy of $E_p = 1912$ keV, 30 keV above the reaction threshold. With this choice of E_p , neutrons are kinematically collimated into a forward cone of 120 deg opening angle. The effect of fluctuations in beam intensity can be corrected by monitoring the neutron yield throughout the irradiations by means of a ${}^6\text{Li}$ -glass detector.

With typical beam intensities of $100 \mu\text{A}$, neutron intensities of $3 \times 10^9 \text{ s}^{-1}$ can be reached, orders of magnitude higher than in time of flight (TOF) experiments. Accordingly, the activation method offers unique sensitivity. Further advantages are (i) that isotopically enriched samples are not required, because the reaction products are identified by their characteristic γ radiation, and (ii) that contributions from the direct radiative capture (DRC) channel are automatically considered. A sketch of the experimental setup and the comparison of the resulting quasi-stellar neutron spectrum with a true Maxwell-Boltzmann distribution are shown in Fig. 3.

The series of activation measurements by Heil *et al.* [7] produced some surprises: While the results for ${}^{58}\text{Fe}$ and ${}^{59}\text{Co}$ confirmed the previously recommended MACS values [6], substantial differences between 20 and 70% were obtained for ${}^{64}\text{Ni}$, ${}^{63}\text{Cu}$, and ${}^{65}\text{Cu}$, thus confirming the need for checking all MACS data for the weak s process.

The revised cross sections gave rise to the differences in the abundance distribution shown in Fig. 4, where the ratio is plotted between the initial distribution and the one obtained with the improved cross section results. The reverse behavior compared to the case of ${}^{62}\text{Ni}$ originates from the fact that the MACS values of ${}^{64}\text{Ni}$, ${}^{63}\text{Cu}$, and ${}^{65}\text{Cu}$ were found to be smaller than assumed before, thus hampering the reaction flow and inducing a negative propagation effect.

The thin solid lines in Fig. 4 illustrate the uncertainties resulting from the extrapolation of the MACS values from the thermal energy of $kT = 25$ keV covered by the measurements to $kT = 90$ keV typical of the higher temperature during the subsequent shell carbon burning phase. Below mass 70 to 75, these uncertainties are clearly limiting the results obtained with the activation method. Consequently, complementary time-of-flight (TOF) experiments are required to define the energy-differential cross section, $\sigma(E_n)$, towards higher energies, preferentially up to about 300 keV.

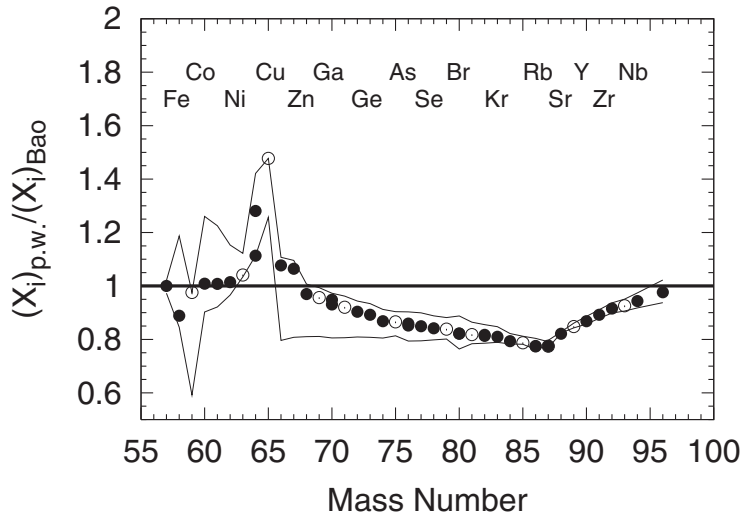


Fig. 4. Comparison of s -process yields between Fe and Nb for a $25 M_{\odot}$ star obtained with the previous set of MACS values [10] and with the updates provided by Heil *et al.* [7]. The thin lines indicate the uncertainties due to the upper and lower MACS limits resulting from the extrapolation of the measured cross sections to the thermal energy of $kT = 90$ keV during the shell carbon burning phase.

3 Time-of-flight experiments

TOF measurements are essential for defining energy-differential neutron capture cross sections over a sufficiently large energy range that MACS values can be determined from these data for any stellar temperature of interest. Recent developments and improvements in pulsed neutron sources and detection techniques have led to (n, γ) cross section measurements with improved accuracy, in many cases with uncertainties of 2 - 4%. Although current measurements by the n_TOF collaboration will be used here to illustrate the state-of-the-art in the field of TOF measurements, the broader context will be sketched as well.

As far as the laboratory neutron sources are concerned, spallation reactions induced by energetic particle beams constitute the most prolific pulsed sources of fast neutrons for TOF measurements. Presently, two such spallation sources are in routine operation, LANSCE at Los Alamos [11] and the n_TOF facility at CERN [12]. The main advantage of these facilities is the outstanding efficiency for neutron production due to the high primary proton beam energies of 800 MeV and 20 GeV at LANSCE and n_TOF, respectively. At n_TOF, for example, 300 neutrons are produced per incident proton, which makes this facility the most luminous white neutron source presently available.

Spallation sources are operated at rather low repetition rates while still maintaining high average intensities. The situation at LANSCE is characterized by a comparably short flight path of 20 m, a time resolution of 250 ns, and a repetition rate of 50 Hz, similar to the performance of the J-PARC complex in Japan [13]. The n_TOF facility at CERN, however, is providing higher resolution in neutron energy (185 m flight path, 7 ns pulse width) and even lower repetition rates of typically 0.4 Hz [12].

The spectrum of keV neutron facilities includes also small accelerators, where neutrons are produced by nuclear reactions, such as the ${}^7\text{Li}(p, n){}^7\text{Be}$ reaction, which offer the possibility of tailoring the neutron spectrum exactly to the stellar energy range. It has been shown that limitations in source strength can be compensated by low backgrounds and the use of comparably short neutron flight paths [14, 15]. High intensities can also be achieved via (γ, n) reactions at electron linear accelerators, such as GELINA at Geel, Belgium, by bombarding heavy metal targets with electron beams of typically 50 MeV. Also these facilities provide excellent resolution in neutron energy and have been extensively used to study the resolved resonance region [16].

Current measurements of (n, γ) cross sections are based on two types of detectors. Total absorption calorimeters are designed to detect the full energy sum of the γ -ray cascade emitted in the decay of

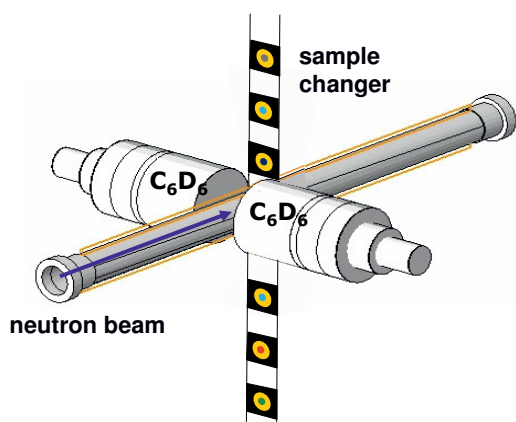


Fig. 5. Sketch of the experimental setup showing the evacuated neutron beam lines, the C_6D_6 detectors, and the sample changer. The neutron beam enters from the left.

the compound nucleus, which corresponds essentially to the binding energy of the captured neutron. Because the neutron separation energy represents the best signature of a capture event, 4π detectors with an efficiency close to 100% are the most direct way to unambiguously identify (n, γ) reactions and to determine capture cross sections with good accuracy. Calorimeters consisting of large 4π arrays are designed either in spherical geometry, using BaF_2 crystals arranged in a fullerene-type configuration where each module covers the same solid angle with respect to the central sample [17–19], or in a barrel-type geometry, where the sample is surrounded by layers of hexagonal crystals [20,21].

The main problem in using calorimeter type detectors arises from their response to neutrons scattered in the sample. Although the BaF_2 scintillator is selected to consist of nuclei with small (n, γ) cross sections, about 10% of the scattered neutrons are captured in the scintillator. The resulting background can easily be handled in measurements of smoothly varying cross sections, but may complicate the analysis of resonance-dominated cross sections.

The problem of neutron sensitivity is largely avoided by using comparably small, hydrogen-free liquid scintillators in combination with the pulse-height weighting technique (PHWT) [22]. In particular since the second generation of detectors, which are based on deuterated benzene (C_6D_6) has been designed with emphasis on minimizing the construction materials and on replacing aluminum and steel by graphite or carbon fiber, backgrounds due to direct interaction of scattered neutrons in the detector became practically negligible [23]. With advanced Monte Carlo codes, realistic descriptions of the detector response and of the weighting functions (WF) could be determined on the basis of detailed computer models of the experimental setup [16,24–26]. A dedicated set of measurements at the n.TOF facility confirmed that WFs obtained by such refined simulations allow one to determine neutron capture cross sections with a systematic accuracy of better than 2% [25].

Accordingly, a setup with two optimized C_6D_6 detectors has been adopted by the n.TOF collaboration for measuring the (n, γ) cross sections of the stable Fe and Ni isotopes, corresponding to the seed nuclei of the weak s process in massive stars and its immediate progeny [27]. This experimental campaign aims at the determination of the energy-differential cross sections, $\sigma(E_n)$, in the entire neutron energy range needed for obtaining the MACS values up to a thermal energy of $kT = 90$ keV.

A sketch of the experimental setup is shown in Fig. 5. During the experiments the neutron flux was monitored slightly upstream of the sample position by counting the ${}^6Li(n, t){}^4He$ reactions produced in a thin 6Li deposit on a Mylar foil with four large Si detectors outside the neutron beam [28]. The prompt capture γ rays were detected with two optimized C_6D_6 liquid scintillation detectors [23].

The metallic samples (20 mm in diameter and ≈ 2 g in mass) are placed in a narrow gap between the thin KAPTON windows of the evacuated the beam pipes. The Fe and Ni samples with isotopic enrichments between 96 and 99.9% were glued onto a KAPTON foil stretched over a carbon fibre frame which is not hit by the neutron beam. The use of a sample ladder enabled easy exchange of

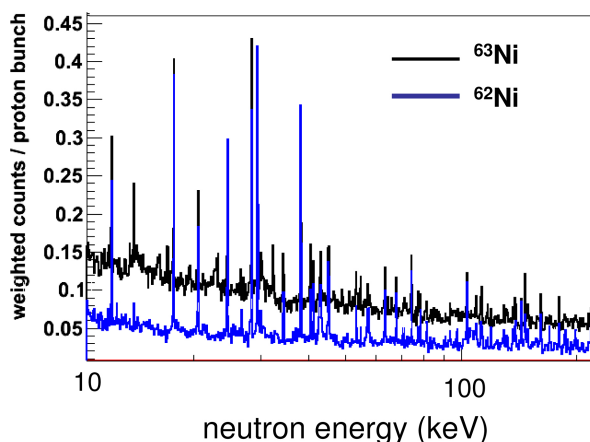


Fig. 6. Spectra taken at n_TOF with a pure ^{62}Ni sample (lower spectrum) and with a ^{62}Ni sample containing about 12% ^{63}Ni (upper spectrum). Resonances can be resolved even at neutron energies well above 200 keV.

samples for calibration and background measurements. In addition to the enriched Fe and Ni samples, Au, Pb, and C served for the determination of the neutron flux and of the backgrounds due to in-beam γ rays and sample scattered neutrons, respectively.

For each neutron burst the detector signals were continuously recorded with fast digitizers (500 MS/s) over periods of 16 ms starting from the impact of the proton pulse on the spallation target. The detector noise was suppressed by the data acquisition software and the waveform of the remaining true signals was analyzed by a pulse fitting procedure, which provided precise amplitude and TOF values of each signal, even in conditions of moderate pile-up. This information was then stored for later data processing.

In addition to the stable Fe and Ni isotopes, a ^{62}Ni sample containing about 12% of the radioactive isotope ^{63}Ni with a half-life of 101 yr has been studied as well. The MACS of this isotope is important because ^{63}Ni represents a branching point, which diverts in the reaction flow to pass preferentially through $^{63}\text{Cu}/^{64}\text{Zn}$ or through ^{65}Cu , depending on neutron density. The sample was available as NiO because it had been cleaned before the measurement from the decay product ^{63}Cu ; it and contained 811 and 108 mg of ^{62}Ni and ^{63}Ni , respectively.

The data taken during the n_TOF campaign are presently under analysis. The excellent quality of the data is illustrated in Fig. 6, which shows the TOF spectra taken with pure ^{62}Ni and with the mixed $^{62}\text{Ni}/^{63}\text{Ni}$ sample. Both spectra exhibit clearly resolved resonances even at neutron energies well above 200 keV. The MACS values, which will be eventually derived from the n_TOF campaign are expected to settle most of the problems related to the the extrapolation issues indicated in Fig. 4.

4 Experiments on ^{60}Fe : technological frontiers

The origin of ^{60}Fe is important for a number of reasons: It was found to contribute substantially to the Galactic γ -radioactivity measured with satellite-based instruments [29]. These observations found that relatively short-lived isotopes produced in explosive nucleosynthesis events such as novae (^{22}Na) and supernovae (^{44}Ti) appear as point sources typically correlated with remnants of the specific explosive

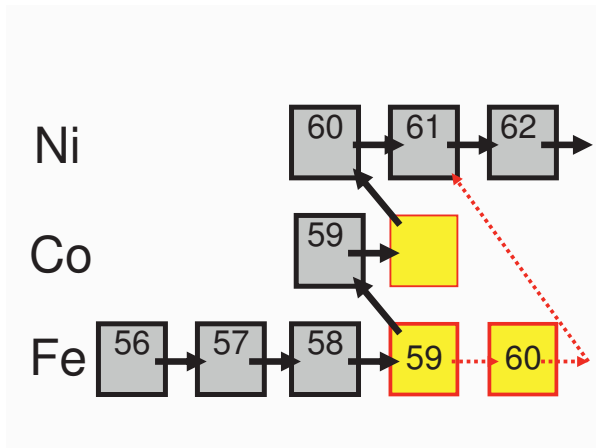


Fig. 7. The s -process reaction path to ^{60}Fe via the branching at ^{59}Fe ($t_{1/2} = 44.5$ d). Note that ^{60}Fe is produced only at the high neutron densities reached during the shell carbon burning phase (dashed arrows). The decay of ^{60}Co is omitted here because it is much slower than the time scale of the s process, but eventually it contributes to the ^{60}Ni abundance.

event. A second class of long-lived γ -ray emitters such as $^{26}\text{Al}^g$ and ^{60}Fe are characterized by a diffuse distribution along the galactic plane with the spatial profile of the emission reflecting the Galactic distribution of a large number of sources. The isotopes $^{26}\text{Al}^g$ and ^{60}Fe are mainly produced in massive stars with $M \geq 8M_{\odot}$ under both pre-explosive and explosive conditions [30–32]. Prior to the supernova explosion, $^{26}\text{Al}^g$ is synthesized via proton capture during core/shell H- and shell C-burning, while ^{60}Fe is produced by neutron capture reactions in the high neutron fluxes reached during shell C-burning. The pre-supernova $^{26}\text{Al}^g$ and ^{60}Fe abundances are subsequently modified by the supernova explosion before being ejected into the interstellar medium.

Observations from space with the γ -ray satellites RHESSI [33] and INTEGRAL [34] yielded $^{60}\text{Fe}/^{26}\text{Al}^g$ ratios of 0.097 ± 0.039 and 0.11 ± 0.03 , which have been confronted with models for element production in massive stars. Apart from the importance of the reaction rates associated with the production and depletion of $^{26}\text{Al}^g$ and ^{60}Fe , the simulations showed that the isotopic ratios depend critically on the choice of the initial mass function (IMF) and of the mass loss rate [30, 31].

The enrichment of ^{60}Ni in meteoritic inclusions [35–38] indicates that ^{60}Fe has been present in substantial amounts in the early solar system and has been taken as evidence for early injection of ^{60}Fe from a nearby supernova into the protosolar nebula [39–42]. In this context, ^{60}Fe represents an important chronometer for the early solar system (ESS) [43].

Furthermore, the discovery of ^{60}Fe in deep sea manganese crusts [44] implies that fresh ^{60}Fe was injected into the solar system 2.8 Myr ago by a nearby supernova when the solar system swept through the expanding SN envelope. The $^{60}\text{Fe}/^{56}\text{Fe}$ ratio of 2.4×10^{-16} measured by accelerator mass spectrometry (AMS) could in principle be used to determine the distance of the SN, an important constraint for the impact of this event on the terrestrial biosphere.

As mentioned before, a significant contribution to the interstellar ^{60}Fe abundance is provided by the s process during convective shell C-burning in massive stars, where high neutron densities are produced by the $^{22}\text{Ne}(\alpha, n)^{25}\text{Mg}$ reaction [3, 45, 46]. Fig. 7 shows that the s -process production of ^{60}Fe , which starts from the most abundant seed nucleus ^{56}Fe , is determined by the branching at ^{59}Fe ($t_{1/2} = 44.5$ d). At the low neutron densities during convective core He burning, ^{60}Fe is shielded from the s -process chain, because the β -decay rate of ^{59}Fe dominates over the (n, γ) rate by orders of magnitude. The branch to ^{60}Fe becomes only efficient during the shell C-burning phase, where higher temperatures of $T = (1.0 - 1.4) \times 10^9$ K give rise to neutron densities in excess of 10^{11} cm^{-3} necessary for bridging the instability gap at ^{59}Fe .

The interpretation of all the above observations depends critically on the reliability of the stellar models as well as on the neutron capture rates for production and depletion of ^{60}Fe [29]. In this mass region, theoretical cross section calculations with the Hauser-Feshbach statistical model are too uncertain in this mass region, because level densities are at the limit to justify the underlying assumptions. Especially in case of ^{60}Fe , the calculated values may vary by an order of magnitude [47].

In the first attempt to measure the (n, γ) cross section of ^{60}Fe [48] the sample turned out to be the major problem, because ^{60}Fe is very difficult to produce. The solution found was to extract ^{60}Fe from a Cu beam dump previously irradiated with 590 MeV protons at the Paul Scherrer Institute (Villigen, Switzerland). Sophisticated radiochemical separation techniques [49] had to be applied to purify the sample to such a high degree that the number of ^{60}Fe atoms could be determined by the in-growing ^{60}Co activity.

The sample produced in this way contained 1.3×10^{16} ^{60}Fe atoms corresponding to a mass of 1.4 μg , much too small for present TOF techniques. Therefore, the activation method described above had been applied using the Karlsruhe 3.7 MV Van de Graaff accelerator with typical beam intensities of 100 to 150 μA . Depending on the performance of the ^7Li targets a neutron source strength of $(2 - 4) \times 10^9 \text{ s}^{-1}$ was obtained.

Because of the short half life of ^{61}Fe ($t_{1/2} = 5.98 \pm 0.06 \text{ min}$ [50]), the experiment was divided into 47 repeated irradiations. The irradiations lasted for 15 min, followed by a transfer time of about 60 s from the irradiation position to the counting station, where the activity was measured for 10 min. The ^{60}Fe sample was sandwiched between 0.03 mm thick gold foils for determination of the time integrated neutron flux.

The small sample and the small cross section resulted in induced activities that were extremely difficult to measure. The γ -rays emitted in the decay of ^{61}Fe were counted with a pair of heavily shielded HPGe clover detectors, each with a relative efficiency of 120%. By arranging the detectors face to face in very close geometry, absolute peak efficiencies of 26% and 10% could be achieved for the prominent γ lines at 298 and 1027 keV, respectively. The positions of the detectors and of the sample were exactly defined by a special sample holder to ensure that the counting geometry was reproducible within $\pm 0.1 \text{ mm}$.

The intrinsic γ -ray background of the sample presented a serious problem for the activity measurements. At low energies, the γ -spectrum was dominated by internal bremsstrahlung from the decay of the ^{55}Fe impurity, thus impeding the 298 keV line expected to show the best signature for the decay of ^{61}Fe . At higher energies, the detection of the stronger lines at 1027 and 1205 keV was limited by the lower detection efficiency and natural background. This problem could be overcome by making use of the eight-fold segmentation of the Ge clover array [51]. Requiring coincidence detection of the 298/1027 keV cascade transitions provided excellent background suppression. The nearly background free spectrum shown in Fig. 8 could be obtained, however, only at the expense of detection efficiency, resulting in a large statistical uncertainty of 14%. Nevertheless, the stellar (n, γ) cross section of ^{60}Fe at 25 keV thermal energy could be determined to $5.7 \pm 1.1_{\text{syst}} \pm 0.8_{\text{stat}} \text{ mbarn}$. This value is lower than in the original paper [48] because the sample mass had to be corrected for the revised half life of ^{60}Fe [52].

This result represents an important step for defining the contribution of the weak s process to the production of ^{60}Fe in massive stars. However, the corresponding information for the higher temperatures and neutron densities during the shell carbon burning phase as well as the respective cross sections for ^{59}Fe needs still to be determined. At present, the measured ^{60}Fe cross section can be used to guide theoretical calculations of the missing data on the basis of the Hauser-Feshbach statistical model, although this approach will be less reliable than further measurements.

Possibilities for obtaining the cross section at higher energies are activations in modified quasi-stellar spectra [53] or TOF measurements. In both cases, one has to face a significant reduction in neutron flux. While the first possibility needs still to be tested, estimates for TOF measurements show that the flux at present facilities is much too low, unless larger samples become available. Given the sample at hand, one finds that the fluxes of the upgraded n.TOF facility at CERN (planned) as well as at the new Frankfurt neutron source (under construction [54,55]) would still be too low by two and one order of magnitude, respectively. Furthermore, TOF measurements would require samples of sufficient isotopic enrichment, whereas the available material consists of the isotope mix produced in

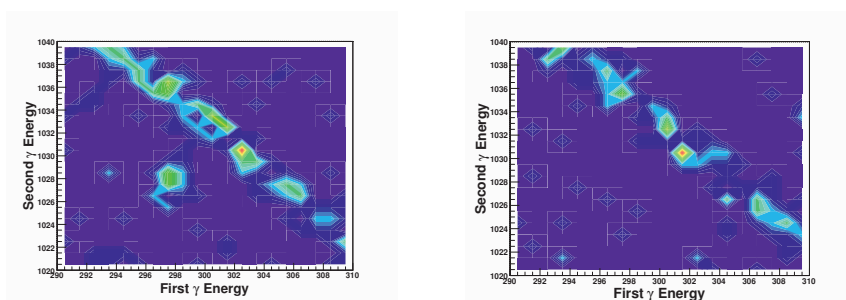


Fig. 8. Left: Coincidence spectrum of the 298-1027 keV cascades in the decay of ^{61}Fe . Right: Intrinsic backgrounds. The diagonal feature in both spectra corresponds to events with multiplicity two originating from scattering of the 1332 keV ^{60}Co line.

the spallation process. Accordingly, further experimental progress requires solutions of the problems related to the TOF facilities as well as to the production of a suited sample. Correspondingly, these problems will be even more complicated for the short-lived branch point isotope ^{59}Fe .

5 Summary

The slow neutron capture process in massive stars contributes substantially to the element abundances in the mass region between Fe and Zr. This scenario is characterized by neutron production via $^{22}\text{Ne}(\alpha, n)$ reactions during the core He and shell C burning stages of stellar evolution. Neutron capture cross sections in the keV region are the key quantities for describing the isotopic abundance pattern originating from this site. These data are the more important as the integrated neutron flux is too weak for establishing flow equilibrium in the reaction chain. Consequently, uncertainties of single cross sections result in a propagation wave, which affects the abundances of many subsequent isotopes. Considerable uncertainties and obvious discrepancies in the stellar (n, γ) cross sections have motivated a number of measurements, especially for the isotopes in the Fe to Zn region, either using the activation technique [7] or high resolution time-of-flight methods [27], which have produced very promising results already.

In this context, observations of live [29,52] and extinct [41] ^{60}Fe have created enormous interest in the origin of this unstable isotope ($t_{1/2} = 2.6$ Myr) and hence in its stellar (n, γ) cross section. Although it turned out that a suited sample was extremely difficult to obtain, a batch of ^{60}Fe could be claimed by means of sophisticated radiochemical purification techniques from a Cu beam dump for 590 MeV protons [49]. The recovered amount was just sufficient for an activation measurement. To complement this first result with more comprehensive time-of-flight measurements represents a true challenge for the most intense pulsed neutron sources and would also require the production of an isotopically enriched sample of ^{60}Fe .

References

1. E. Burbidge, G. Burbidge, W. Fowler, and F. Hoyle, *Rev. Mod. Phys.* **29**, 547 (1957).
2. R. Gallino *et al.*, *Ap. J.* **497**, 388 (1998).
3. C. Raiteri *et al.*, *Ap. J.* **419**, 207 (1993).
4. T. Rauscher, A. Heger, R. Hoffman, and S. Woosley, *Ap. J.* **576**, 323 (2002).
5. M. Arnould and S. Goriely, *Phys. Rep.* **384**, 1 (2003).
6. I. Dillmann, R. Plag, F. Käppeler, and T. Rauscher, in *EFNUDAT Fast Neutrons - scientific workshop on neutron measurements, theory & applications* (JRC-IRMM, Geel, 2009), <http://www.kadonis.org>.

7. M. Heil *et al.*, Phys. Rev. C **78**, 025802 (2008).
8. H. Beer and F. Käppeler, Phys. Rev. C **21**, 534 (1980).
9. W. Ratynski and F. Käppeler, Phys. Rev. C **37**, 595 (1988).
10. Z. Bao *et al.*, Atomic Data Nucl. Data Tables **76**, 70 (2000).
11. P. Lisowski, C. Bowman, G. Russell, and S. Wender, Nucl. Sci. Eng. **106**, 208 (1990).
12. U. Abbondanno *et al.*, Technical report, CERN, Geneva, Switzerland, (unpublished), report CERN-SL-2002-053 ECT.
13. <http://j-parc.jp/>, Technical report, JAERI and KEK (unpublished).
14. K. Wisshak and F. Käppeler, Nucl. Sci. Eng. **77**, 58 (1981).
15. Y. Nagai *et al.*, Ap. J. **381**, 444 (1991).
16. P. Koehler *et al.*, Phys. Rev. C **54**, 1463 (1996).
17. K. Wisshak, K. Guber, F. Käppeler, and F. Voss, Nucl. Instr. Meth. A **299**, 60 (1990).
18. M. Heil *et al.*, Nucl. Instr. Meth. A **459**, 229 (2001).
19. R. Reifarh *et al.*, Nucl. Instr. Meth. A **531**, 530 (2004).
20. K. Guber, R. Spencer, P. Koehler, and R. Winters, Nucl. Phys. **A621**, 254c (1997).
21. J. Klug *et al.*, Nucl. Instr. Meth. A **577**, 641 (2007).
22. R. Macklin, Nucl. Sci. Eng. **95**, 200 (1987).
23. R. Plag *et al.*, Nucl. Instr. Meth. A **496**, 425 (2003).
24. J. Tain, F. Gunsing, D. Cano-Ott, and C. Domingo, J. Nucl. Sci. Tech. Suppl. **2**, 689 (2002).
25. U. Abbondanno *et al.*, Nucl. Instr. Meth. Phys. Res. A **521**, 454 (2004).
26. A. Borella *et al.*, in *International Conference on Nuclear Data for Science and Technology*, edited by R. Haight, M. Chadwick, T. Kawano, and P. Talou (AIP, New York, 2005), pp. 652–655, AIP Conference Series 769.
27. C. Lederer, G. Giubrone, *et al.*, (unpublished).
28. S. Marrone *et al.*, Nucl. Instr. Meth. Phys. Res. A **517**, 389 (2004).
29. R. Diehl, N. Prantzios, and P. von Ballmoos, Nucl. Phys. **A777**, 70 (2006).
30. F. Timmes *et al.*, Ap.J. **449**, 204 (1995).
31. M. Limongi and A. Chieffi, Ap. J. **647**, 483 (2006).
32. S. Woosley and A. Heger, Phys. Rep. **442**, 269 (2007).
33. D. Smith, New Astron. Rev. **48**, 87 (2004).
34. M. Harris *et al.*, Astron. Astrophys. **433**, L49 (2005).
35. J. Birck and G. Lugmair, Earth Planet. Sci. Lett. **90**, 131 (1988).
36. G. Quitté *et al.*, Ap. J. **655**, 678 (2007).
37. Y. Guan, G. Huss, and L. Leshin, Geochim. Cosmochim. Acta **71**, 4082 (2007).
38. F. Moynier *et al.*, Geochim. Cosmochim. Acta **71**, 4365 (2007).
39. S. Mostefaoui, G. Lugmair, and P. Hoppe, Astrophys. J. **625**, 271 (2005).
40. L. Looney, J. Tobin, and B. Fields, Astrophys. J. **652**, 1755 (2006).
41. N. Dauphas, . Cook, . Sacarabany, and Fr .
42. N. Ouellette, S. Desch, and J. Hester, Astrophys. J. **662**, 1268 (2007).
43. A. Boss, Astrophys. J. **660**, 1707 (2007).
44. K. Knie *et al.*, Phys. Rev. Lett. **93**, 171103 (2004).
45. C. Raiteri, M. Busso, R. Gallino, and G. Picchio, Ap. J. **371**, 665 (1991).
46. M. Limongi, O. Straniero, and A. Chieffi, Ap. J. Suppl. **129**, 625 (2000).
47. T. Rauscher and F.-K. Thielemann, Atomic Data Nucl. Data Tables **75**, 1 (2000).
48. E. Uberseder *et al.*, Phys. Rev. Lett. **102**, 151101 (2009).
49. D. Schumann *et al.*, Nucl. Instr. Meth. A, **613**, 347 (2010).
50. M. Bhat, Nucl. Data Sheets **88**, 417 (1999).
51. R. Reifarh *et al.*, Ap. J. **582**, 1251 (2003).
52. G. Rugel *et al.*, Phys. Rev. Lett. **103**, 072502 (2009).
53. P. Mastinu, G. Martín Hernández, and J. Praena, Nucl. Instr. Meth. A **601**, 333 (2009).
54. R. Reifarh *et al.*, Publications of Astronomical Society of Australia **26**, 255 (2009).
55. C. Wiesner *et al.*, in *Proceedings of the VIII Latin American Symposium on Nuclear Physics and Applications*, <http://link.aip.org/link/?APC/1265/487/I>, edited by R. Alarcon *et al.*, AIP Conference Proceedings 1265, p. 487 (2010).